Extreme Mechanics Letters 79 (2025) 102398

Contents lists available at ScienceDirect

Extreme Mechanics Letters

journal homepage: www.elsevier.com/locate/eml

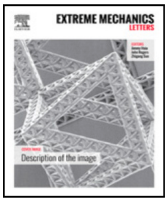

Pull-in instability of droplet amplified electrostatic actuators considering dielectric barrier discharge

Delei Qin [a], Jianglong Guo [a],*, Yanju Liu [b], Jinsong Leng [c]

[a] School of Science, Harbin Institute of Technology (Shenzhen), Shenzhen, 518055, Guangdong, China
[b] Department of Astronautical Science and Mechanics, Harbin Institute of Technology, Harbin, 150001, Heilongjiang, China
[c] Center for Composite Materials and Structures, Harbin Institute of Technology, Harbin, 150001, Heilongjiang, China

ARTICLE INFO

Keywords:
Liquid-amplified electrostatic actuator
Dielectric barrier discharge
Pull-in instability

ABSTRACT

Liquid-amplified electrostatic actuators can generate greater forces than conventional ones which use air as the dielectric between two electrodes. Dielectric droplet amplified electrostatic actuators, a major type of liquid amplified electrostatic actuator, can be used to provide powerful, fast, energy-efficient, and lightweight actuations. However, the mechanical response of droplet amplified electrostatic actuator and the liquid amplification mechanism remain unexplored in a comprehensive way. Here we present a quasi-static model for droplet amplified electrostatic actuators considering dielectric barrier discharge and capillary force. The Galerkin method and the Newton method were used to numerically solve the model. A customized pull-in voltage measurement setup was established to verify the numerical results and the main influencing parameters were studied. The experimentally validated model can be used to accurately predict the quasi-static response and pull-in voltage of droplet amplified electrostatic actuators. This work highlights that the liquid amplification comes mainly from higher permittivity than air, dielectric barrier discharge elimination, and capillary force, due to the use of liquid dielectrics instead of air. The results in this work may provide useful insights into droplet amplified electrostatic actuator structural optimization, control, and application.

1. Introduction

Electrostatic actuators employ attractive or repulsive Coulomb forces between two conducting electrodes when there is a potential difference between them [1–9], and they usually feature low energy consumption, fast response, lightweight, and can be easily controlled [1–9], compared to other alternative controllable actuators [10–27]. There exists an air gap between two insulated electrodes for conventional electrostatic actuators [1–3] and this results relatively small displacements and forces, significantly limiting their uses.

Hydraulically amplified electrostatic actuators employ dielectric liquids that have larger dielectric permittivity and greater breakdown strength than air, thus producing greater electrostatic forces [28]. A typical example is the hydraulically amplified self-healing electrostatic (HASEL) actuator [28] that has been used for robotic gripping [29,30], wearable haptics [31,32], mobile robots [33–35], shape display [36], among others. Another example is the dielectrophoretic liquid zipping (DLZ) actuator [37] which only uses a droplet of dielectric liquid, resulting lighter and easier-to-make structures that can be used for robotic gripping [37–39], mobile robots [37], flexible pumps [40,41], artificial muscle [42], etc. Previous results and models, including the electromechanical model of electro-ribbon actuators [43], all simply suggest that the liquid amplification mainly comes from the use of liquid dielectric who has higher permittivity than air [37,38,43–45].

A recent application of DLZ actuators is the liquid-amplified zipping actuator (LAZA) for flying robots [45,46] which do not require any transmission system. A typical LAZA actuator prototype can be shown in Fig. 1(a) (fabrication materials and process can be seen in the Appendix A) and the schematic diagram of the actuator structure is shown in Fig. 1(a), mainly consisting of a rigid insulated curved electrode, a deformable electrode, and a dielectric droplet. Like other electrostatic actuators [47–56], LAZA based direct drives may also suffer from pull-in instability that will significantly affect their actuating or flapping performance [47–49,51,55,56]. There is, however, a lack of investigation into pull-in instability of dielectric droplet amplified electrostatic actuators (DAEA).

As shown in Fig. 1(a), high-voltage (in the range of kV [40]) induced dielectric discharge may occur in DAEAs [57] and dielectric barrier discharge (dielectric discharge after dielectric breakdown) [58–67] may easily happen because of the dielectric insulator. There is lack of accurate analytical descriptions of dielectric barrier discharge

---

* Corresponding author.
E-mail address: guojianglong@hit.edu.cn (J. Guo).

https://doi.org/10.1016/j.eml.2025.102398
Received 17 December 2024; Received in revised form 28 June 2025; Accepted 13 August 2025

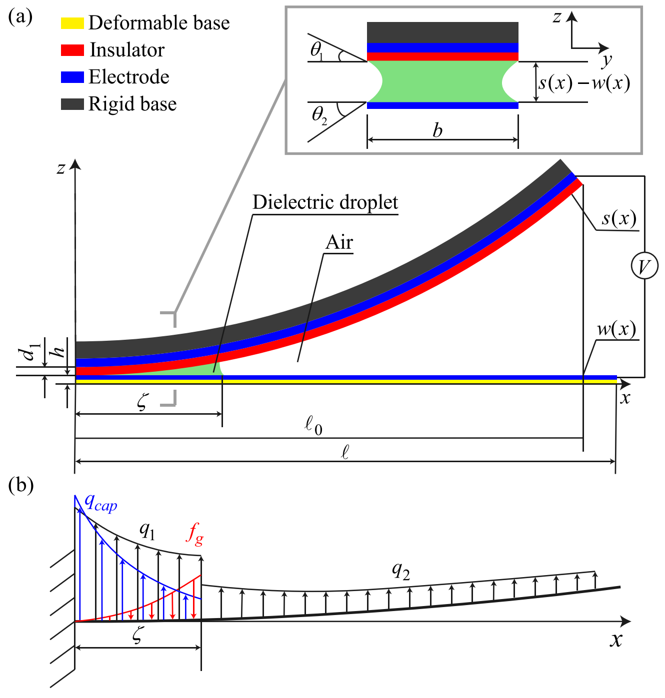

Fig. 1. DAEA components and model. (a) Schematic diagram of the DAEA with geometric parameters. (b) Deformed electrode subjected to distributed forces.

due to the complex physical mechanism [58–69]. Current traditional parallel-plate electrostatic force models usually ignore high-voltage induced dielectric barrier discharge. Pull-in voltage model that neglects dielectric barrier discharge may bring inaccurate predictions.

In response, based on the LAZA structure as shown in Fig. 1(a), we firstly present a DAEA model, based on a macro-scale phenomenological parallel-plate electrostatic force model, considering dielectric barrier discharge and capillary force. We then calculate the DAEA pull-in voltage numerically and establish a pull-in instability characterization rig to experimentally validate the numerical results. After this, we present discussions on both experimental and theoretical results. Specifically, Section 2 introduces the model, the boundary conditions, and numerical solution method of DAEAs. Section 3 details the experimental methods, platform, and electrostatic force results that can be used to build the dielectric barrier discharge considered parallel-plate electrostatic force model which can be applied to calculate the pull-in voltage and quasi-static response of the actuator. Section 4 sums up the main findings of this work.

2. The DAEA model

As shown in Fig. 1(a), the DAEA consists of a rigid insulated electrode, a deformable electrode and a drop of liquid dielectric. When there is a potential difference between the rigid insulated electrode and the deformable electrode, the deformable electrode is pulled towards the rigid electrode due to electrostatic forces. The rigid electrode consists of a rigid base, an electrode and an insulator, and the deformable electrode consists of a deformable base and an electrode. The length, width and thickness of the deformable electrode are ℓ, b and h, respectively. The deflection of the deformable electrode is $w(x)$. The curve function of the rigid electrode is $s(x)$ and the length along the z-axis direction is ℓ_0. The thickness of the insulator is d_1. The contact angle between the droplet and the insulator is θ_1 and between the droplet and the deformable electrode is θ_2. The boundary between the droplet and air is ζ.

2.1. Governing equation and boundary conditions

We consider the deformation of the deformable electrode as a cantilever due to distributed forces (see Fig. 1(b)). It is assumed that the non-stretchable electrode is a linear elastic geometrically nonlinear Euler–Bernoulli beam, so the transverse shear deformation and the variation of cross-sectional dimensions are neglected, and the deformation satisfies the Kirchhoff assumption [70], then the governing equation can be written as (detailed derivation is given in Appendix B):

$$EI\left((1+w'^2)w'''' + 4w'w''w''' + w''^3\right) + \rho gbh = f \tag{1}$$

where E is the Young's modulus of the deformable electrode, I is the second moment of area of the deformable electrode (the material parameters of the deformable electrode equal approximately to the materials of the deformable base as shown in Appendix A), ρ is the density of the deformable electrode, and g is the gravitational acceleration. The second moment of area of deformable electrode can be written as $I = 1/12\ \mathrm{bh}^3$. The distributed force f, combining electrostatic forces q_1 (the dielectric is liquid dielectric) and q_2 (the dielectric is air), capillary adhesion forces q_{cap} [71–74], and the gravity of the dielectric droplet f_g, can be written as:

$$f = \begin{cases} q_1 + q_{cap} - f_g, x < \zeta \\ q_2, \zeta \le x < \ell_0 \\ 0, \ell_0 \le x < \ell \end{cases} \tag{2}$$

where $q_{cap} = \gamma b(\cos\theta_1 + \cos\theta_2)/(s(x)-w(x))$, $f_g = \rho_0 gb(s(x)-w(x))$, γ is the surface tension coefficient and ρ_0 is the density of the dielectric liquid. The surface tension of the droplet is so small that the contact angle between the droplet and the insulator θ_1 and the contact angle between the droplet and the deformable electrode θ_2 can be set to zero. Then capillary force can then be written as $q_{cap} = 2\gamma b/(s(x)-w(x))$.

The boundary conditions for the deformable electrode are:

$$w(0) = 0, w'(0) = 0, w''(\ell) = 0, w'''(\ell) = 0 \tag{3}$$

There is a dynamic boundary condition between the dielectric droplet and air:

$$\Omega_0 = \int_0^\zeta (s(x)-w(x))\,bdx \tag{4}$$

where Ω_0 is the droplet volume.

2.2. Numerical solution

Given that the electrostatic force is related to the applied voltage V, the distributed force can be expressed as $f = f(w,x,V,\zeta)$, Eq. (1) can then be written as:

$$EI[(1+w'^2)w'''' + 4w'w''w''' + w''^3] + \rho gbh = f(w,x,V,\zeta) \tag{5}$$

We firstly expand the deflection function by a series:

$$w(x) = \sum_{i=1}^{n} c_i\varphi_i(x) \tag{6}$$

where $\varphi_i(x)$ is a set of basic functions that satisfy the boundary conditions (Eq. (3)) and c_1 are the ratios. We then used the Galerkin method to solve the Eq. (5):

$$\begin{aligned}
&\int_0^\ell \varphi_1(x)(EI[(1+w'^2)w'''' + 4w'w''w''' + w''^3] + \rho gbh)dx = \\
&\int_0^\ell \varphi_1(x)f(w,x,V,\zeta)dx \\
&\int_0^\ell \varphi_2(x)(EI[(1+w'^2)w'''' + 4w'w''w''' + w''^3] + \rho gbh)dx = \\
&\int_0^\ell \varphi_2(x)f(w,x,V,\zeta)dx \\
&\vdots
\end{aligned}$$

$$\int_0^{\ell} \varphi_n(x)(EI[(1+w'^2)w'''' + 4w'w''w''' + w''^3] + \rho gbh)dx = \int_0^{\ell} \varphi_n(x) f(w, x, V, \zeta)dx \tag{7}$$

where:

$$\begin{aligned} w'(x) &= \sum_{i=1}^{n} c_i \varphi_i'(x) \\ w''(\ell) &= \sum_{i=1}^{n} c_i \varphi_i''(\ell) \\ w'''(\ell) &= \sum_{i=1}^{n} c_i \varphi_i'''(\ell) \\ w''''(\ell) &= \sum_{i=1}^{n} c_i \varphi_i''''(\ell) \end{aligned} \tag{8}$$

There are $n+2$ unknown numbers in Eq. (7), $c_1, c_2 \ldots c_n, \zeta$ and V. The endpoint deflection of the deformable electrode is:

$$w(\ell) = \sum_{i=1}^{n} c_i \varphi_i(\ell) \tag{9}$$

By combining the Eqs. (4), (7) and (9) and solving them iteratively using the Newton method, we can obtain the relationship between the applied voltage V and the endpoint deflection of the deformable electrode $w(\ell)$ at equilibrium.

3. Results and discussions

In this section, we analyze the effect of dielectric barrier discharge on macro-scale parallel-plate electrostatic forces and build a phenomenological parallel-plate electrostatic force model considering dielectric barrier discharge. Then we use both theoretical and experimental methods to analyze the pull-in instability of the actuator and explain the amplification mechanism of dielectric droplet in detail. Finally, we analyze the influence of different physical parameters of DAEA on the pull-in voltage.

3.1. Parallel-plate electrostatic force model considering dielectric barrier discharge

It is relatively difficult to compute the dynamic electrostatic force because of the continuous geometrical variation along the x-axis within the DAEA as shown in Fig. 1. To simplify the calculation of electrostatic force, we use piece-wise parallel-plate elements and the classical parallel-plate electrostatic force between piece-wise parallel-plate elements can be described as:

$$q = \frac{\varepsilon_0 \varepsilon_{r2} A V^2}{2(d_1 \frac{\varepsilon_{r2}}{\varepsilon_{r1}} + d_2)^2} \tag{10}$$

where ε_0 is the vacuum permittivity, d_1 is the thickness of the insulator, ε_{r1} is the permittivity of the insulator, d_2 is the thickness of the dielectric (air or liquid), ε_{r2} is the permittivity of dielectric, and A is the area of electrode. Please be noted that the dielectrics are assumed to be linear, uniform, and homogeneous materials.

Classical parallel-plate electrostatic force model usually does not take dielectric discharge into account. Centimetre scale electrostatic actuators, however, usually require kilovolts to drive them, and this may bring potential dielectric discharges. As for the actuator structure shown in Fig. 1, dielectric barrier discharge (DBD) [58] will occur due to the existence of the insulator. Currently, there is a lack of parallel-plate electrostatic force model considering dielectric discharge for macro-scale electrostatic actuators. Since the dielectric discharge mechanism is complex and it is challenging to directly integrate dielectric discharge theories into Eq. (10), we establish a phenomenological parallel-plate electrostatic force model that considers dielectric discharge by using experimental data and the Eq. (10).

3.1.1. Experimental setup and results

In order to analyze the influence of dielectric discharge on electrostatic force, we established a customized parallel-plate electrostatic force measurement setup (as shown in Fig. 2(a)) to measure electrostatic forces when the dielectric is air or liquid. We used a high voltage power supply (AMPS-20B20, Matsusada Precision, Japan) to provide high voltages to the electrodes that induce electrostatic forces measured by a load cell (Series no. 55 900, Richmond Industries, UK). A data acquisition (DAQ) device (USB-6001, National Instruments, USA) was used to record the force data and control the voltage output of the high voltage power supply. A laser displacement sensor (LK-500, Keyence, Japan and LK-H150, Keyence, Japan) was used to test the thickness of dielectric. A direct current power supply (DP832A, RIGOL Technologies, China) was used to power the load cell.

The parallel-plate electrostatic force test structure consists two plate electrodes. One is the insulated plate electrode which consists of a base, an electrode and an insulator. The other is no insulated plate electrode which only consists of an electrode and a base. The size of the plate electrode is $100\,\mathrm{mm} \times 100\,\mathrm{mm}$. The insulated plate electrode was made of a 3D printed base, made of polylactic acid (PLA), bonded with a stretchable electrode (ARcare 90 366, Adhesives Research, USA) that was covered with a polyvinyl chloride (PVC) tape (No.223S, Nitto, Japan) with permittivity of 5.21 and thickness of $0.19\,\mathrm{mm}$. The test structure was placed in the tank where air and a silicone oil (PMX 200, Xiameter, USA) were used. The permittivity of silicone oil was 2.7 and the permittivity of air was 1.

The voltage applied to the test structure was linearly increasing. We compared different voltage increase rates (as shown in Fig. 2(b)), including $10\,\mathrm{V/s}$, $100\,\mathrm{V/s}$ and $1000\,\mathrm{V/s}$, and found that the electrostatic force increase followed almost the same trend, so we adopted $100\,\mathrm{V/s}$ for the parallel-plate electrostatic force measurement. Because the dielectric discharge was related to the thickness of dielectric (d_2), we tested electrostatic force at different thicknesses. The thickness was measured by the laser displacement sensor. The measurement setup is shown in Appendix C. We conducted the tests when the temperature was 22.3 ± 0.4 °C and relative humidity was 68 ± 2%.

We compared the theoretical results calculated by Eq. (10) and experimental results of electrostatic force when the dielectric was air/liquid (silicone oil), as shown in Fig. 2(c). It can be easily found that when the dielectric was liquid the theoretical results were very close to experimental results, so the classical parallel-plate electrostatic force model was still applicable. However, when the dielectric was air, the theoretical results and experimental results gradually changed from close to not close with the increase of applied voltage, so the classical parallel-plate electrostatic force model was not applicable.

3.1.2. Macro-scale phenomenological parallel-plate electrostatic force model

Due to the classical parallel plate electrostatic force model is applicable when the dielectric is liquid, we only considered the influence of air discharge in the electrostatic force. It is shown in Fig. 2(c), when the dielectric is air and the applied voltage is small, the experimental results are very close to the theoretical results. When the applied voltage is large enough, the rate of increase in the experimental results gradually decreases compared to the theoretical results. The reason is that the surface charge accumulated in the insulator surface from air discharge generated a reverse electric field opposite to the direction of the applied electric field [58–67]. We established an empirical model by considering the surface charge accumulated in the insulator surface.

Here we assume that: (1) the dielectrics are assumed to be linear, uniform, and homogeneous materials; (2) the density of surface charges accumulated in the dielectric surface is assumed to be homogeneous; and (3) the influence of the edge effect of electric fields and free electrons in air are neglected.

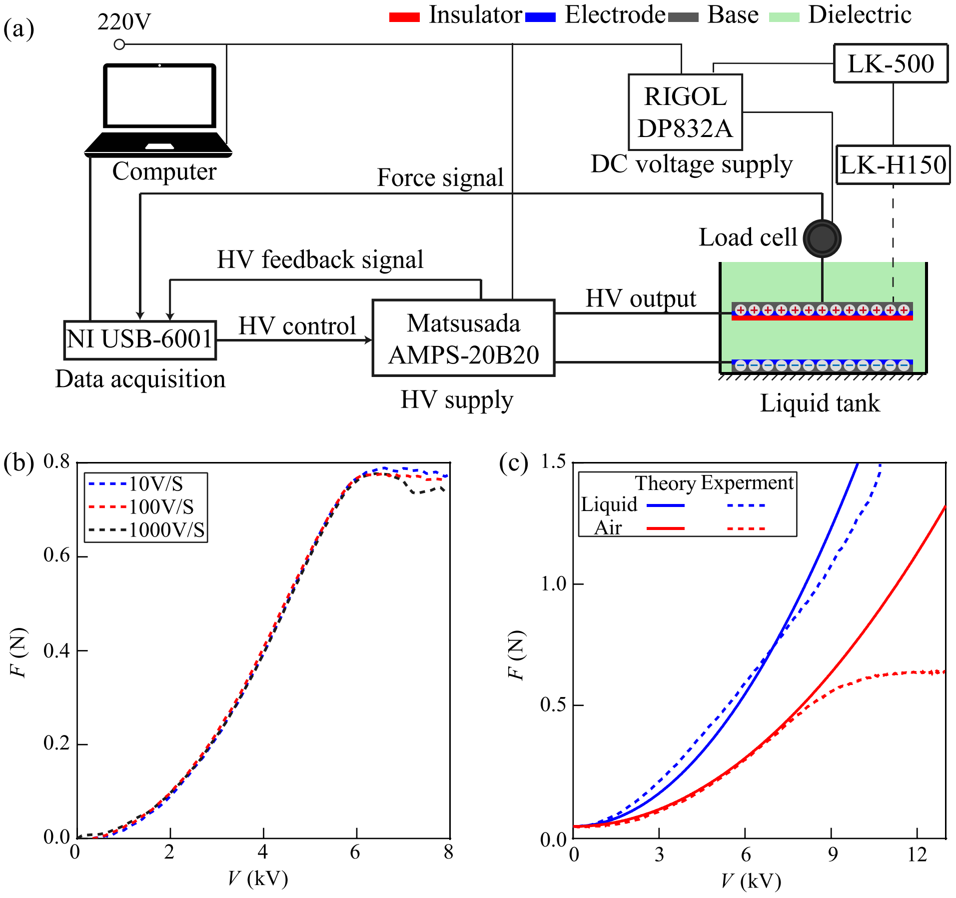

Fig. 2. Parallel-plate electrostatic force measurement considering dielectric barrier discharge. (a) Schematic diagram of the parallel-plate electrostatic force measurement setup. (b) Relationship between parallel-plate electrostatic force and voltage increasing rate. (c) Comparison of classical parallel-plate electrostatic force model and experimental results when the dielectrics are air and silicone oil.

The parallel-plate test structure (as shown in Fig. 2) can be modeled as two capacitors connected in series. Consequently, the total applied voltage is:

$$V = E_1 d_1 + E_2 d_2 \tag{11}$$

where E_1 and E_2 are the electric field in insulator and dielectric. According to the normal component of the electric displacement field:

$$\varepsilon_0 \varepsilon_{r1} E_1 - \varepsilon_0 \varepsilon_{r2} E_2 = \sigma_s \tag{12}$$

where σ_s is the surface free charge density on the insulator surface. Solve Eqs. (11) and (12), the electric field in dielectric layer can be written as:

$$E_2 = \frac{V - \sigma_s \frac{d_1}{\varepsilon_0 \varepsilon_{r1}}}{d_2 + \varepsilon_{r2} \frac{d_1}{\varepsilon_{r1}}} \tag{13}$$

According to the Maxwell stress tensor, the parallel plate electrostatic force can be calculated as:

$$F = \frac{1}{2} \varepsilon_0 \varepsilon_{r2} A E_2^2 = \frac{1}{2} \varepsilon_0 \varepsilon_{r2} A \left(\frac{V - \sigma_s \frac{d_1}{\varepsilon_0 \varepsilon_{r1}}}{d_2 + \varepsilon_{r2} \frac{d_1}{\varepsilon_{r1}}} \right)^2 \tag{14}$$

There is no analytical model to calculate the relationship between the insulator surface free charge and the applied voltage. Some studies have shown that the free-charge density initially follows a power-law increase with the applied voltage [75], but at sufficiently high voltages the insulator surface free-charge density transitions to a linear dependence [68]. This is consistent with our electrostatic force measurements: once the applied voltage exceeds the critical breakdown voltage of the dielectric, a barrier discharge occurs and the accumulated surface free charges produce a reverse electric field, which slows the growth of the electrostatic force. At very high voltages, this force ultimately levels off and remains essentially constant. In order to describe the relationship between the charge density and the applied voltage, we established a new fitted model (here we called it as the variable–exponent power (VEP) model):

$$\sigma_s(V) = \begin{cases} 0, & V < V_{bk} \\ K(V - V_{bk})^{\left(\frac{V - V_{bk}}{V - V_{bk} + \alpha}\right)}, & V \geq V_{bk} \end{cases} \tag{15}$$

where E_{bk} is the critical breakdown voltage of dielectric, K and α are the parameters to be fitted, K is the gain of charge density linear growth and α is used to control the transition of charge density growth from nonlinear to linear. The critical breakdown voltage of dielectric can be written as:

$$V_{bk} = E_{bk} \left(d_2 + d_1 \frac{\varepsilon_{r2}}{\varepsilon_{r1}} \right) \tag{16}$$

where E_{bk} is the breakdown electric field of dielectric.

There are various forms of models that satisfy the variation law of insulator surface free change density, so we comprehensively consider the complexity of the model and the fitting effect, and select the VEP model shown in Eq. (15). Comparison of fitting effects of different forms of models is shown in Appendix D. Fig. 3 shows the comparison between the theoretical and experimental results. Table D.1 shows the goodness-of-fit of the empirical model. The coefficient of determination (R^2) and the coefficient of variation of RMSE (RMSE-CV) show that the empirical model has good predictive ability. Root mean squared error (RMSE) and mean absolute error (MAE) are on the order of 10^{-2},

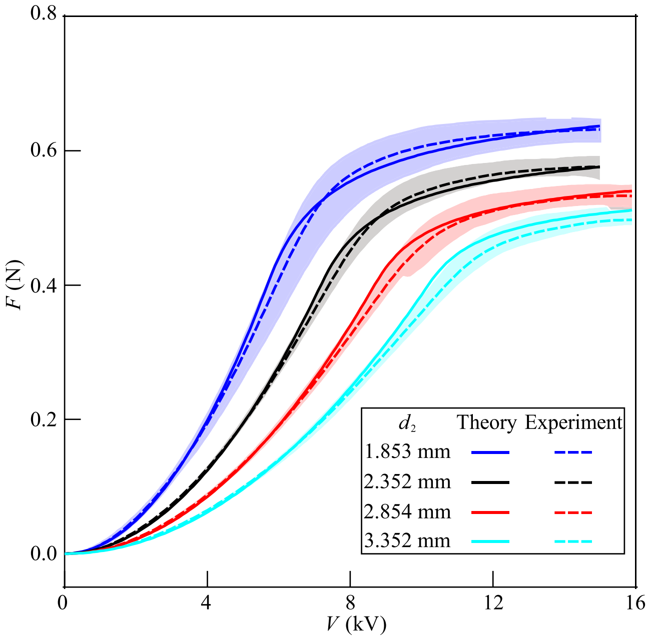

Fig. 3. Comparison of theoretical and experimental results of parallel-plate electrostatic force considering dielectric barrier discharge.

indicating that the error level of the empirical model is very low. Table D.2 shows the fitted parameters of the empirical model.

3.2. DAEA quasi-static response and pull-in voltage

3.2.1. Experimental setup

As shown in Fig. 4(a), we established a customized setup to measure the response and pull-in voltage of the DAEA actuator. We used a high voltage power supply (AMPS-20B20, Matsusada Precision, Japan) to provide high voltages to the actuator. A high speed camera, consisting of an industrial camera (VC-12MX-M180E0-DIN(FM), Vieworks, Korea), a camera mount (DH-ADFM-19, IMAVISION, China), a camera connector (DH-UNIFOC34A, IMAVISION, China), and a camera lens (DH-LS8056A, IMAVISION, China), was used to capture the actuator motions. An image acquisition card (RAP4G4C6, Matrox, Canada) was used to record the image data from the high speed camera. A data acquisition (DAQ) device (USB-6001, National Instruments, USA) was used to record the voltage feedback data and control the voltage output of the high voltage power supply and high speed camera. A direct current power supply (DP832A, RIGOL Technologies, China) was used to power the high speed camera. A LED light (DH-P-RL-100-90-W, IMAVISION, China) and its controller were used to light up the image shooting.

Here we adopted 500 V/s for the quasi-static response and pull-in voltage tests, and the tests were conducted when the temperature was 22.3 ± 0.4 °C and relative humidity was 68 ± 2%. We used digital image processing techniques to obtain the relationship between endpoint deflection and time. Also, we obtained the relationship between voltage and time. Then, through the interpolation method, we achieved the relationship between endpoint deflection and voltage. We then obtained the pull-in voltage when there was a rapid step change (see Fig. 4(c)) in the endpoint deflection. As the applied voltage increases, the endpoint deflection increases until the deformable electrode fully was adhered to the rigid electrode (see Fig. 4(b) and (c)). It is shown in Fig. 4(c) that when the voltage increases in a critical value, the endpoint deflection will increase sharply. This phenomena is called pull-in instability and the critical voltage is called pull-in voltage.

3.2.2. Experimental results and their comparisons with theoretical results

In order to determine the distributed forces $f(w,x,V,\zeta)$, we need to determine the electrostatic force q_1 and q_2 as shown in Eq. (2). From Section 3.1, the electrostatic force (when the dielectric is droplet q_1) can be written as:

$$q_1(w,x,V) = \frac{\varepsilon_0 \varepsilon_{r2} b V^2}{2\left(d_1 \frac{\varepsilon_{r2}}{\varepsilon_{r1}} + s(x) - w(x)\right)^2} \tag{17}$$

The electrostatic force (when the dielectric is air q_2) can be written as:

$$q_2(w,x,V) = \frac{1}{2}\varepsilon_0 \varepsilon_{r2} A \left(\frac{V - \sigma_s \frac{d_1}{\varepsilon_0 \varepsilon_{r1}}}{s(x) - w(x) + \varepsilon_{r2} \frac{d_1}{\varepsilon_{r1}}}\right)^2 \tag{18}$$

We then use the Newton method to solve Eqs. (4), (7) and (9). To simplify the analysis, we make $w_\ell^* = w(\ell)/s(\ell_0)$ and $V^* = V/V_{max}$ as the dimensionless endpoint deflection and dimensionless voltage respectively. Here we take $V_{max} = 10\,\mathrm{kV}$. The relationship between the dimensionless endpoint deflection of the deformable electrode and dimensionless voltage is shown in Fig. 5(a). The voltage required to keep the deformable electrode in the equilibrium state increases first and then decreases as the endpoint deflection increases, and the maximum value is the pull-in voltage. The deformable electrode will adsorb onto the rigid electrode when the applied voltage is larger than the pull-in voltage. The material and physical parameters used to calculation are detailed in Table 1.

In order to validate that the maximum value is the critical point between stability and instability, we used three different applied voltages, $V = 1500\,\mathrm{V}$, $V = 2000\,\mathrm{V}$ and $V = 2500\,\mathrm{V}$, and found the relationship between the dimensionless endpoint deflection and the dimensionless total potential energy, as shown in Fig. 5(b), (c) and (d), where $V = 1500\,\mathrm{V}$ and $V = 2000\,\mathrm{V}$ were less than the pull-in voltage $V_{pull-in}$, and $V = 2500\,\mathrm{V}$ was greater than the pull-in voltage $V_{pull-in}$. The derivation of total potential energy Π is shown in Appendix B and the dimensionless total potential energy is Π/Eh^3. There exists a minimal value of the total potential energy when the applied voltage was less than the pull-in voltage as shown in Fig. 5(b) and (c). The horizontal coordinate of the minimal value is the equilibrium endpoint deflection of the deformable electrode at the applied voltage. When the applied voltage was greater than the pull-in voltage, there is no a minimal value of the total potential energy as shown in Fig. 5(d). The deformable electrodes remain deformed until they are fully absorbed with the rigid electrodes at this voltage.

Fig. 5(e) shows the experimental and theoretical results of the quasi-static response of DAEA and the electrostatic actuator without dielectric droplet. The dielectric droplet can be used reduce the DAEA pull-in voltage. There were four cases adopted to calculate the pull-in voltage, including: (1) the consideration of the influence of dielectric barrier discharge for actuators without dielectric droplet, (2) the neglection of the dielectric barrier discharge for actuators without dielectric droplet, (3) the neglection of the capillary force for DAEAs, (4) the consideration of the influence of the capillary force for DAEAs. It is obvious to see that the theoretical results for the first and fourth cases are more in line with the experimental results.

The comparison of the experimental and theoretical results in different cases reveals that the amplification mechanism of the dielectric droplet comprises three aspects. Firstly, dielectric droplets can be used to eliminate electrostatic force attenuation due to dielectric barrier discharges. Secondly, dielectric liquid droplets have greater permittivity than air. Thirdly, the capillary force of the dielectric droplet contributes to the overall forces. It is shown in Fig. 5(e) that the first and the third have a greater effect than the second on the decrease of the pull-in voltage.

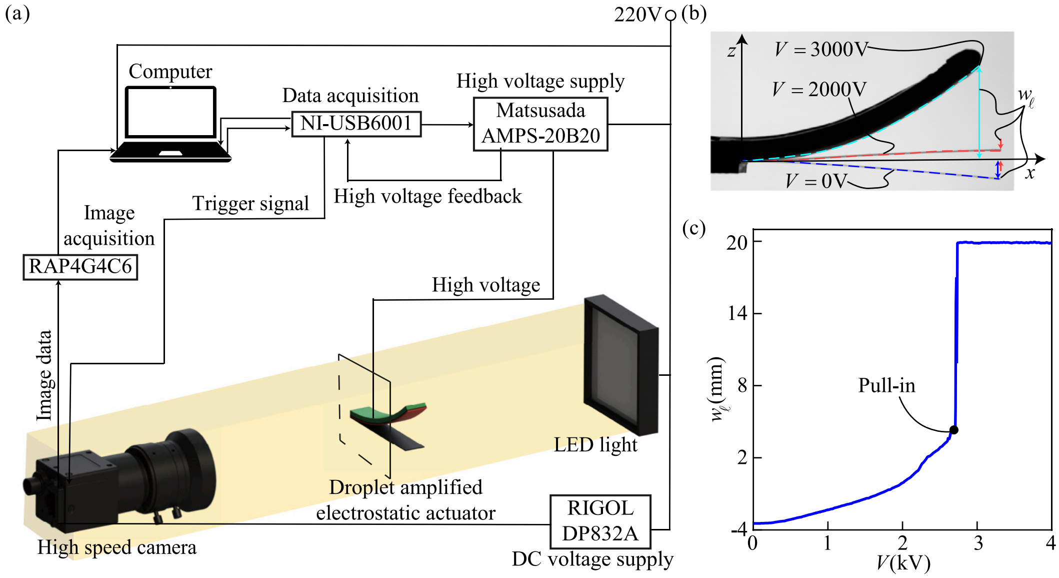

Fig. 4. DAEA quasi-static response an pull-in voltage measurement. (a) Schematic diagram of the DAEA quasi-static response and pull-in instability experimental characterization platform. (b) Quasi-static response of deformable electrode at 0 V, 2000 V and 3000 V (c) Relationship between voltage and endpoint deflection.

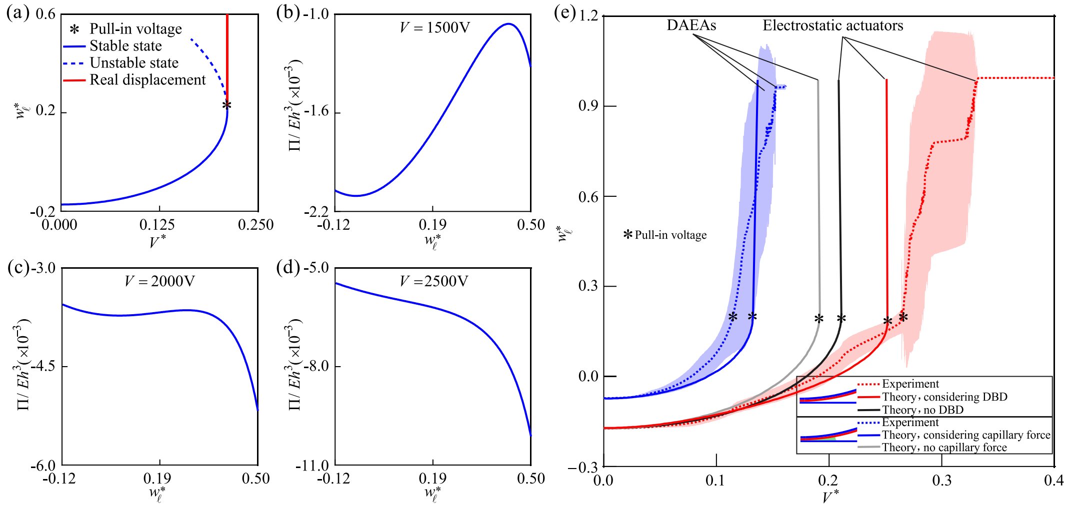

Fig. 5. DAEA quasi-static response and pull-in voltage theoretical and experimental results. (a) Relationship between dimensionless voltage and dimensionless endpoint deflection. (b) Total potential energy when the applied voltage was 1500 V. (c) Total potential energy when the applied voltage was 2000 V. (d) Total potential energy when the applied voltage was 2500 V. (e) Theoretical and experimental results of the actuator with or without the dielectric droplet.

Table 1
Physical parameters of the pull-in voltage calculation.

Parameter	Unit	Value
G	GPa	3.4
b	mm	20
h	mm	0.1
ℓ	mm	45
ℓ_0	mm	40
d_1	mm	0.19
ρ	kg/m^3	1900
ρ_0	kg/m^3	764
γ	mN/m	21
ε_0	F/m	8.85×10^{-12}
ε_{r1}	1	5.21
ε_{r2}	1	2.7
Ω_0	μL	40

3.3. DAEA pull-in voltage influencing parameters

The pull-in instability is caused by the fact that the resistance to deformation of deformable electrode cannot balance the electrostatic force. The physical parameters, which influence the deformation of deformable electrode and electrostatic force, will influence the actuator pull-in voltage. Fig. 6 shows that the theoretical and experimental results of the influence of the volume of dielectric droplet and the thickness of deformable electrode to the pull-in voltage. The thickness of deformable electrode is changed by altering the thickness of the base.

As shown in Fig. 6(a), the pull-in voltage decreases as the volume of droplet increases. The decrease rate decreases as the volume of droplet increases. When the droplet volume is small, the capillary force and dielectric barrier discharge elimination dominate the force amplification, while when the volume is relatively large, the force amplification mainly comes from the permittivity. From Fig. 6(b), we can find that the variations of the pull-in voltage have a significant difference between the actuator with dielectric droplet and without

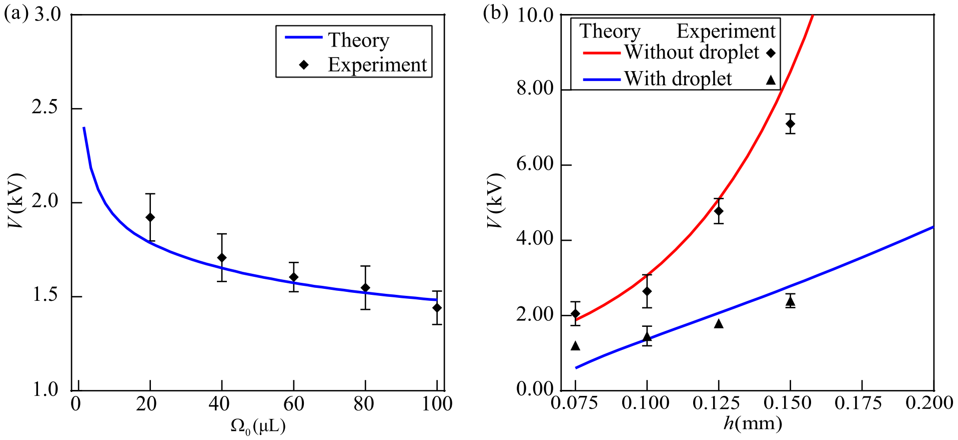

Fig. 6. Comparison of theoretical and experimental results of pull-in voltage. (a) Experimental validation of theoretical results with variable volume of droplet. (b) Experimental validation of theoretical results with variable thickness of deformable electrode.

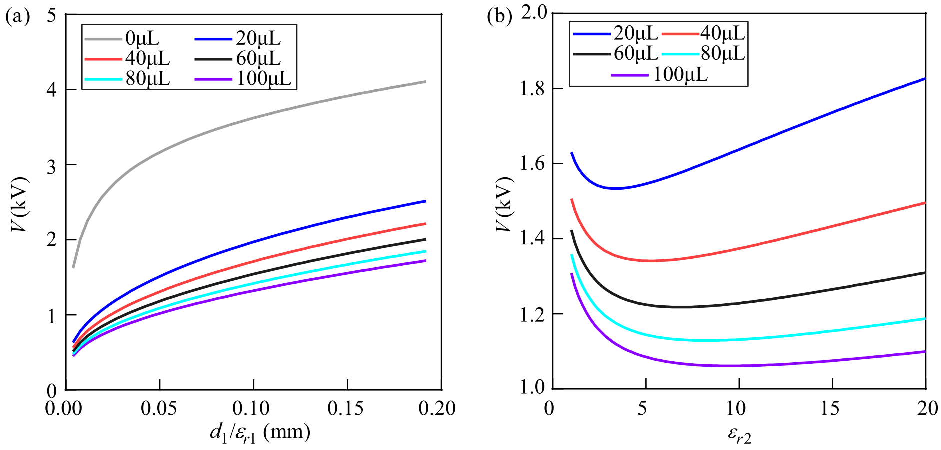

Fig. 7. Theoretical results of pull-in voltage with variable physical parameters at different volumes of droplet. (a) Theoretical results of pull-in voltage with variable physical parameters of insulator d_1/ε_{r1}. (b) Theoretical results of pull-in voltage with variable permittivity of droplet ε_{r2}.

dielectric droplet. The pull in-voltage increase with increasing the thickness of deformable electrode. But the increase rate of the actuator without dielectric droplet is larger than the actuator with droplet. As the thickness of the deformable electrode increases, it requires an higher applied voltage to produce the same deformation. This voltage elevation subsequently induces an expansion in the dielectric barrier discharge area. The enlarged discharge area in turn necessitates higher applied voltage to maintain a specific electrostatic force requirement. This is a positive feedback process. So the pull-in voltage increase rapidly for the actuator without dielectric droplet. But the droplet eliminates the positive feedback. The essential reason why thickness affects the pull-in voltage is the bending rigidity. The Young's modulus E and thickness h thus have similar effects on pull-in voltage.

As shown in Fig. 6, the pull-in voltage theoretical results agreed well with the experimental results. So we can use the model to analyze the influence of other physical parameters to the pull-in voltage. As shown in Fig. 7, we separately analyzed the influence of the physical parameters of insulator d_1/ε_{r1} and permittivity of droplet ε_{r2} to the pull-in voltage.

The pull-in voltage increase with increasing d_1/ε_{r1} and the increase speed decrease as shown in Fig. 7(a). The insulator and dielectric of DAEAs can be regarded as two capacitors connected in series, with equal stored charges under voltage applied. The capacitance of the insulator decreases with increasing d_1/ε_{r1}, and the total capacitance also decreases with increasing d_1/ε_{r1}. While in other conditions unchanged, the amount of charge stored in the dielectric capacitor decreases, resulting in a decrease in electrostatic force and an increase in pull-in voltage. The pull-in voltage firstly decreases and then increases with increasing the permittivity of the droplet as shown in Fig. 7(b). The electrostatic force reaches the maximum value when the permittivity takes $\varepsilon_{r2} = \varepsilon_{r1}(s(x)-w(x))/d_1$. While in other conditions unchanged, the increase of permittivity ε_{d2} will cause the decrease of electric field in dielectric. According to Maxwell stress tensor [76], as the permittivity ε_{d2} increases, the electrostatic force will increase, and as the electric field E decreases, the electrostatic force will decrease. The coupling between the two mechanisms resulted in the changing trend of the pull-in voltage as shown in Fig. 7(b). And the increase rate of the pull-in voltage decreases as the increase of the volume of the droplet. The reason is that the capillary adhesion force increases with the increase of droplet volume, resulting in a decrease in pull-in voltage increase rate.

4. Conclusion

In this work, we have completed the first pull-in instability study of DAEAs. We integrated the first phenomenological parallel-plate electrostatic force model considering dielectric barrier discharge into the DAEA quasi-static model. We used the Galerkin method and the Newton method to numerically solve the pull-in voltage. We also developed a customized DAEAs pull-in instability test rig to experimentally verify the theoretical results. The theoretical results agreed quite well with the experimental results. Key finding of this work includes:

(1) When the dielectric is air, dielectric barrier discharge will decrease the increase rate of parallel-plate electrostatic forces, so the classical electrostatic force model is no longer applicable. The parallel-plate electrostatic force model considering surface charge accumulated on the dielectric surface is applicable. The VEP model, used to fit the insulator surface free charge density, has similar goodness-of-fit with the fewest parameters compared to the PLS and PW models. When the dielectric is liquid, the liquid discharge has little effect on the electrostatic force and the classical parallel-plate electrostatic force model is applicable.

(2) Both theoretical and experimental results showed that the liquid amplification comes mainly from higher permittivity than air, dielectric barrier discharge elimination, and capillary force, due to the use of liquid dielectrics instead of air, and the later two contribute more on force amplification than the higher permittivity.

(3) The pull-in voltage is influenced by $V\ (E, h, \Omega_0, d_1, \varepsilon_{r1}, \varepsilon_{r2})$. Increasing the electrode bending stiffness (EI) can increase the pull-in voltage. The width of deformable electrodes (b) has little effect, but the Young's modulus (E) and thickness of deformable electrodes (h) have a significant impact on the pull-in voltage. Increasing the droplet volume can decrease the pull-in voltage. Increasing d_1/ε_{r1} can decrease the pull-in voltage. In addition, increasing the oil permittivity can firstly decrease and then increase the pull-in voltage.

Future work may include but is not limited to: (1) the investigation into many key performance parameters of DAEAs, such as output force, response time, and energy efficiency, (2) the investigation into the influence of the coupling of electric and fluid field, and (3) the investigation into the dynamic response and dynamic pull-in instability of DAEA.

CRediT authorship contribution statement

Delei Qin: Writing – original draft, Validation, Software, Methodology, Investigation, Formal analysis, Conceptualization. **Jianglong Guo:** Writing – review & editing, Writing – original draft, Validation, Supervision, Methodology, Investigation, Funding acquisition, Formal analysis, Conceptualization. **Yanju Liu:** Writing – review & editing, Supervision, Funding acquisition. **Jinsong Leng:** Writing – review & editing, Supervision, Funding acquisition.

Declaration of competing interest

The authors declare that they have no known competing financial interests or personal relationships that could have appeared to influence the work reported in this paper.

Acknowledgments

This work was supported by the National Natural Science Foundation of China under grant no. 12102106. Also, we thank the support from the Shenzhen Science and Technology Program, China under grant no. JCYJ20210324120212034. In addition, we appreciate Prof. Fei Jia for the helpful discussions on theoretical considerations. Furthermore, we thank Prof. Jonathan Rossiter's inspiration on the mechanics of LAZA actuators.

Appendix A. DAEA manufacturing

The DAEA as shown in Fig. 1(a) consists of a rigid insulated curved electrode, a deformable electrode, and a dielectric droplet. The insulated curve-shaped electrode was made of a 3D printed rigid base, made of polylactic acid (PLA) with its shape function of $s(x) = x^2/2\ell_0$ (where $\ell_0 = 40\,\mathrm{mm}$), bonded with a stretchable electrode (ARcare 90 366, Adhesives Research, USA) that was covered with a polyvinyl chloride (PVC) tape (No.223S, Nitto, Japan) with permittivity of 5.21 and thickness of 0.19 mm. The deformable electrode was made by laser cutting of a polyester (PET) film (ShengHong Petrochemical, China) bonded with the Arcare 90 366 electrode. The stretchable electrode faced the insulating layer was de-adhesioned using talc powders (Tianjin Zhonglian Chemical Reagent Co. Ltd, China). The dielectric droplet was placed by a pipette filled with a silicone oil (PMX 200, Xiameter, USA) with permittivity of 2.7, density of $764\,\mathrm{kg/m^3}$, and viscosity of 10 cSt.

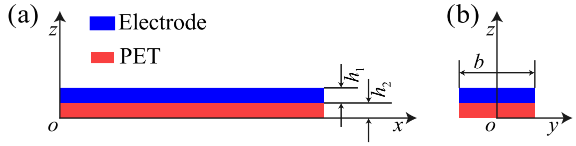

Fig. A.1. Cross-section of the deformable electrode. (a) Perpendicular to the y-axis cross-section. (b) Perpendicular to the x-axis cross-section.

It should be noted that although the deformable electrode was a bilayer structure, the equivalent flexural rigidity can be approximated as the flexural rigidity of the polyester film. The bilayer structure is shown in Fig. A.1. The thicknesses of the electrode and PET were h_1 and h_2, respectively. The widths of the electrode and PET were b. The Young's modulus of the electrode and PET were E_1 and E_2, respectively. The equivalent bending rigidity can be written as:

$$D_{eq} = E_1 I_{1,eq} + E_2 I_{2,eq} \tag{A.1}$$

where D_{eq} is the equivalent bending rigidity, $I_{1,eq}$ is the equivalent second moment of area of the electrode, and $I_{2,eq}$ is the equivalent second moment of area of the PET.

The neutral axis of the bilayer structure is:

$$z_{neu} = \frac{E_1 b_1 h_1 (h_1 + \frac{h_2}{2})}{E_1 b_1 h_1 + E_2 b_2 h_2} \tag{A.2}$$

Rewrite the Eq. (A.2) as:

$$z_{neu} = \frac{(h_1 + \frac{h_2}{2})}{1 + \frac{E_2 h_2}{E_1 h_1}} + \frac{\frac{h_2}{2}}{1 + \frac{E_1 h_1}{E_2 h_2}} \tag{A.3}$$

The Young's modulus of PET is in the GPa range and the Young's modulus of electrode is in the kPa range, so $E_1 \ll E_2$. Also, the thickness of the electrode and PET are in the same range. The neutral axis can thus be written as:

$$z_{neu} \approx \frac{d_2}{2} \tag{A.4}$$

The equivalent second moment of area of the electrode and PET are:

$$\begin{aligned} I_{1,eq} &= \frac{1}{12} b h_1^3 + b h_1 \left(z_{neu} - \left(h_2 + \frac{h_1}{2} \right) \right)^2 \\ I_{2,eq} &= \frac{1}{12} b h_2^3 + b h_2 \left(z_{neu} - \frac{h_2}{2} \right)^2 \end{aligned} \tag{A.5}$$

Due to $E_1 \ll E_2$, the equivalent second moment of area can be written as:

$$D_{eq} \approx \frac{1}{12} E_2 \mathrm{b} h_2^3 \tag{A.6}$$

In summary, the bending rigidity of the deformable electrode EI refers to the bending rigidity of PET film.

Appendix B. Derivation of the governing equation

The total potential energy of the deformable electrode can be described as:

$$\Pi = \Pi_s + G - W \tag{B.1}$$

where Π is the total potential energy of the deformable electrode, Π_s is the strain energy of the deformable electrode, G is the gravitational potential of the deformable electrode, and W is the work of the distributed force.

The strain energy of the deformable electrode can be written as:

$$\Pi_s = \int_\Omega \frac{1}{2}\sigma_{ij}\epsilon_{ij}d\Omega \tag{B.2}$$

where σ_{ij} is the stress of the deformable electrode, ϵ_{ij} is the strain of the deformable electrode and Ω is the volume of the deformable electrode. We assume that the linear elastic non-stretchable electrode is a geometrically nonlinear Euler–Bernoulli beam [70]; then the displacement-strain relationship of the deformable electrode can be written as:

$$\epsilon_{xx} = -z(w'' + \frac{1}{2}w'^2w'') \tag{B.3}$$

where z is the lateral coordinates of the deformable electrode, w is the deflection of the deformable electrode, w' is the first derivative of the deflection of the deformable electrode, and w'' is the second derivative of the deflection of the deformable electrode. Submit Eqs. (B.3) into (B.2), the strain energy can be written as:

$$\Pi_s = \int_\Omega \frac{1}{2}E[-z(w''+\frac{1}{2}w'^2w'')]^2d\Omega = \int_0^\ell \frac{1}{2}EI(w''+\frac{1}{2}w'^2w'')^2dx \tag{B.4}$$

The gravitational potential of the deformable electrode is:

$$G = \int_\Omega \rho gwd\Omega = \int_0^\ell \rho gbhwdx \tag{B.5}$$

The work of the distributed force can be written as:

$$W = \int_0^\ell \int_0^{w(x)} f(w_0)dw_0dx \tag{B.6}$$

Submit Eqs. (B.4)–(B.6) into Eq. (B.1), we have:

$$\Pi = \int_0^\ell \left(\frac{1}{2}EI(w'' + \frac{1}{2}w'^2w'')^2 + \rho gbhw - \int_0^{w(x)} f(w_0)bdw_0\right)dx \tag{B.7}$$

Based on the principle of minimum potential energy, we have:

$$\delta\Pi = \delta\Pi_s + \delta G - \delta W = 0 \tag{B.8}$$

The variation of the strain energy is:

$$\begin{aligned}\delta\Pi_s &= \frac{\partial\Pi_s}{\partial w'}\delta w' + \frac{\partial\Pi_s}{\partial w''}\delta w'' \\ &= \int_0^\ell EI\left(w'' + \frac{1}{2}w'^2w''\right)\left(w'w''\delta w' + \left(1 + \frac{1}{2}w'^2\right)\delta w''\right)dx \\ &= \int_0^\ell \frac{1}{4}EI((4+6w'^2)w''^3 + 8w'(2+w'^2)w''w''' + (2+w'^2)^2w'''') \\ &\quad \delta wdx\end{aligned} \tag{B.9}$$

The variation of the gravitational potential is:

$$\delta G = \frac{\partial G}{\partial w}\delta w = \int_0^\ell \rho gbh\delta wdx \tag{B.10}$$

The variation of the external potential energy is:

$$\delta W = \frac{\partial W}{\partial w}\delta w = \int_0^\ell f\delta wdx \tag{B.11}$$

Substituting Eqs. (B.9)–(B.11) into Eq. (B.8), we get:

$$\frac{1}{4}EI((4+6w'^2)w''^3+8w'(2+w'^2)w''w'''+(2+w'^2)^2w'''')+\rho gbh = f \tag{B.12}$$

Neglecting the high-order infinitesimal terms in Eq. (B.12), we finally get the governing equation:

$$EI((1+w'^2)w'''' + 4w'w''w''' + w''^3) + \rho gbh - f = 0 \tag{B.13}$$

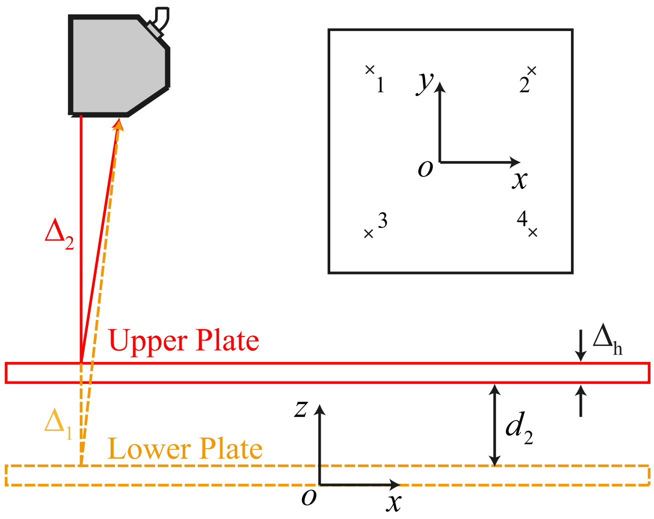

Fig. C.1. Measurement setup of the dielectric thickness.

Table D.1
Goodness-of-fit of different models.

Model	Params	R^2	RMSE	MAE	CV-RMSE
VEP model	2	0.9950	1.485×10^{-2}	1.093×10^{-2}	4.67%
PLS model	3	0.9949	1.554×10^{-2}	1.105×10^{-2}	4.72%
PW model	3	0.9955	1.470×10^{-2}	1.085×10^{-2}	4.46%

Table D.2
Parameters of different models.

Model	K	α	m	V_{tr}
VEP model	4.67×10^{-8}	193.843		
PLS model	1.942×10^{-11}	8.575×10^{-5}	2.256	
PW model	1.225×10^{-8}		1.309	4293.592

Appendix C. Measurement setup of the dielectric thickness

Fig. C.1 shows the measurement setup of the thickness of dielectric. First, we tested the distance between the lower pad and the sensor $\varDelta_1$. Then we determined the distance between the upper pad and the sensor $\varDelta_2$. The thickness of the upper pad h_2 was tested by a micrometer (DL321025B, Deli, China). We chose four points at the same location in the two plates and $\varDelta_h$ is the average value at the four points. The thickness of dielectric d_2 can be calculated as $d_2 = \varDelta_1 - \varDelta_2 - \varDelta_h$.

Appendix D. Comparison of the goodness-of-fit with different models

There are different forms of the insulator surface free charge density model. Here we compare the goodness-of-fit of these models. The first model is the VEP model as shown in Eq. (15). The second model is the power-law suppression (PLS) model:

$$\sigma_s(V) = \begin{cases} 0, & V < V_{bk} \\ \frac{K(V-V_{bk})^m}{\alpha+(V-V_{bk})^{m-1}}, & V \geq V_{bk} \end{cases} \tag{D.1}$$

where K, m and α are the parameters to be fitted, K is the gain of charge density linear growth, m is used to control the shape of the in charge density nonlinear growth curve, and α is used to control the transition of charge density growth from nonlinear to linear. The piece-wise (PW) model can also be used to fit the charge density:

$$\sigma_s(V) = \begin{cases} 0, & V < V_{bk} \\ K(V - V_{bk})^m, & V_{bk} \leq V < V_{tr} \\ \frac{\varepsilon_0\varepsilon_{r1}}{d_1}(V - V_{tr} + \frac{d_1}{\varepsilon_0\varepsilon_{r1}}K(V_{tr} - V_{bk})^m), & V \geq V_{tr} \end{cases} \tag{D.2}$$

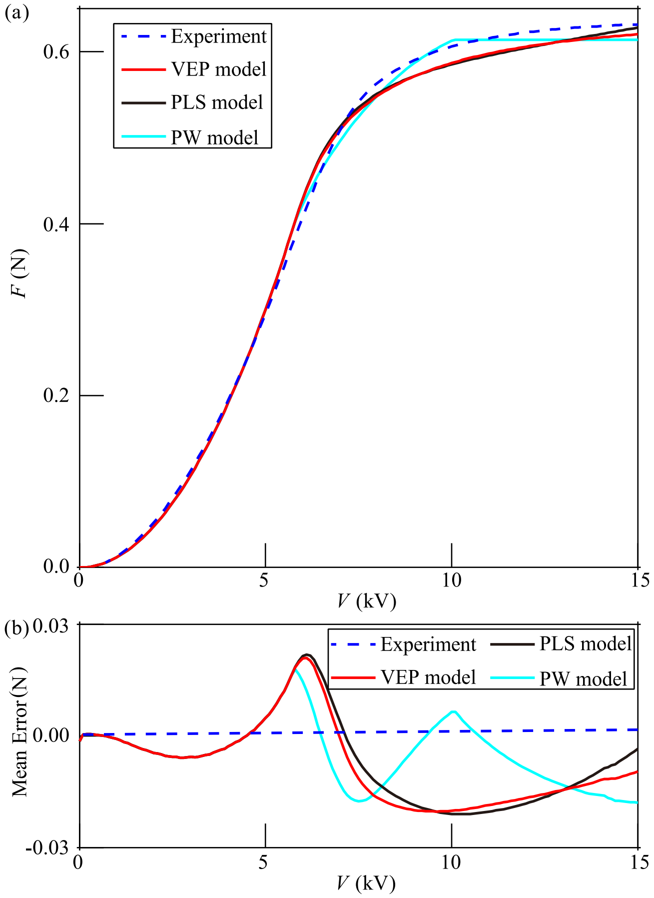

Fig. D.1. (a) Comparison of experimental results and predicted results of electrostatic force with different models of the insulator surface free charge density. (b) Mean error of experimental results and predicted results of electrostatic force with different models of the insulator surface free charge density.

where V_{tr}, K and m are the parameters to be fitted, V_{tr} is the critical voltage between the charge density nonlinear and linear growth, K is the gain of charge density nonlinear growth, and m is used to control the shape of the in charge density nonlinear growth curve.

Fig. D.1(a) shows the $F - V$ comparison of the aforesaid three different insulator surface free charge density models, and Fig. D.1(b) shows the electrostatic force mean error of the models. Table D.1 shows the goodness-of-fit of different models. Table D.2 shows the fitted parameters of different models. Fig. D.1, Tables D.1 and D.2 show that the fits of the three models are very close, but the VEP model has only two parameters to be fitted. Considering the complexity of the model and the fitting effect, we choose the VEP model in this research.

Appendix E. Influence of dielectric liquid viscosity and electrode width

The influence of dielectric liquid viscosity should be neglected for quasi-static analysis. To verify this, we selected three different viscosities, i.e. 5, 10, and 20 cSt, and found that varying liquid viscosities had indeed relatively small effect on quasi-static pull-in voltages (see Fig. E.1(a)). We, therefore, used 10 cSt for all the DAEA pull-in instability

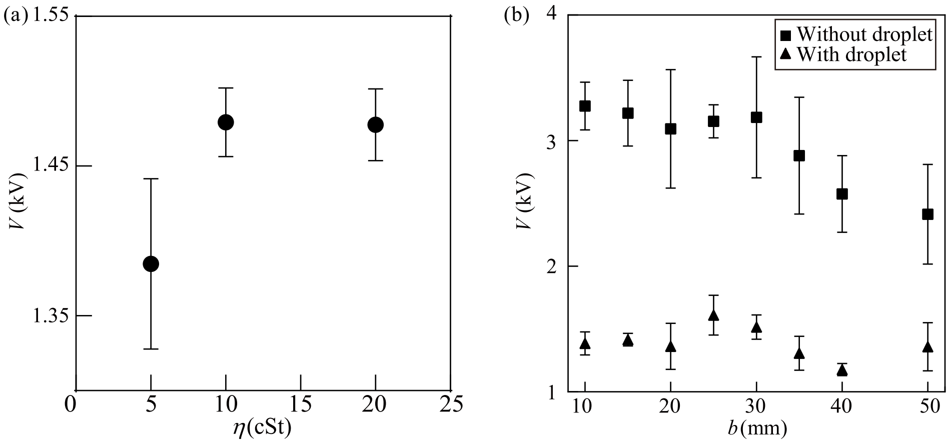

Fig. E.1. (a) Relationship between pull-in voltage and silicone oil viscosity. (b) Relationship between pull-in voltage and electrode width.

experimental tests. Based on the Eq. (1), we can find that the electrode width b can be neglected. To experimentally validate this, we also fabricated actuators with electrode widths of 10, 15, 20, 25, 30, 35, 40, and 50 mm. We found that, as shown in Fig. E.1(b), the influence of electrode width is relatively small, especially when the dielectric is oil.

Data availability

Data will be made available on request.

References

[1] O. Jefimenko, D. Walker, Electrostatic Motors, Electret Scientific Company, 1973, URL https://books.google.com.au/books?id=g08zAAAACAAJ.

[2] C. Jin, J. Zhang, Z. Xu, I. Trase, S. Huang, L. Dong, Z. Liu, S.E. Usherwood, J.X. Zhang, Z. Chen, Tunable, flexible, and resilient robots driven by an electrostatic actuator, Adv. Intell. Syst. 2 (3) (2020) 1900162.

[3] E.W. Schaler, T.I. Zohdi, R.S. Fearing, Thin-film repulsive-force electrostatic actuators, Sensors Actuators A: Phys. 270 (2018) 252–261.

[4] J.D. Grade, H. Jerman, T.W. Kenny, Design of large deflection electrostatic actuators, J. Microelectromech. Syst. 12 (3) (2003) 335–343.

[5] Y. Nemirovsky, O. Bochobza-Degani, A methodology and model for the pull-in parameters of electrostatic actuators, J. Microelectromech. Syst. 10 (4) (2001) 601–615.

[6] W. Lin, Y. Zhao, Nonlinear behavior for nanoscale electrostatic actuators with Casimir force, Chaos Solitons Fractals 23 (5) (2005) 1777–1785.

[7] V. Srikar, S. Spearing, Materials selection for microfabricated electrostatic actuators, Sensors Actuators A: Phys. 102 (3) (2003) 279–285.

[8] V. Leus, D. Elata, Fringing Field Effect in Electrostatic Actuators, Technion-Israel Institute of Technology Technical Report No ETR-2004-2, 2004.

[9] H. Conrad, H. Schenk, B. Kaiser, S. Langa, M. Gaudet, K. Schimmanz, M. Stolz, M. Lenz, A small-gap electrostatic micro-actuator for large deflections, Nat. Commun. 6 (1) (2015) 10078.

[10] X. Liu, H. Ji, B. Liu, Q. Yang, All-solid-state carbon-nanotube-fiber-based finger-muscle and robotic gripper, Int. J. Smart Nano Mater. 13 (1) (2022) 64–78.

[11] M. Li, A. Pal, A. Aghakhani, A. Pena-Francesch, M. Sitti, Soft actuators for real-world applications, Nat. Rev. Mater. 7 (3) (2022) 235–249.

[12] J. Sun, C. Wang, Y. Liu, X. Liang, Z. Wang, Liquid crystal elastomer composites for soft actuators, Int. J. Smart Nano Mater. 14 (4) (2023) 440–459.

[13] P. Polygerinos, N. Correll, S.A. Morin, B. Mosadegh, C.D. Onal, K. Petersen, M. Cianchetti, M.T. Tolley, R.F. Shepherd, Soft robotics: Review of fluid-driven intrinsically soft devices; manufacturing, sensing, control, and applications in human-robot interaction, Adv. Eng. Mater. 19 (12) (2017) 1700016.

[14] C. Chou, B. Hannaford, Measurement and modeling of McKibben pneumatic artificial muscles, IEEE Trans. Robot. Autom. 12 (1) (1996) 90–102.

[15] K.C. Galloway, K.P. Becker, B. Phillips, J. Kirby, S. Licht, D. Tchernov, R.J. Wood, D.F. Gruber, Soft robotic grippers for biological sampling on deep reefs, Soft Robot. 3 (1) (2016) 23–33.

[16] S.H. Sadati, S.E. Naghibi, A. Shiva, Y. Noh, A. Gupta, I.D. Walker, K. Althoefer, T. Nanayakkara, A geometry deformation model for braided continuum manipulators, Front. Robot. AI 4 (2017) 22.

[17] M.C. Yip, G. Niemeyer, High-performance robotic muscles from conductive nylon sewing thread, in: 2015 IEEE International Conference on Robotics and Automation, ICRA, IEEE, 2015, pp. 2313–2318.

[18] S.H. Sadati, L. Sullivan, I.D. Walker, K. Althoefer, T. Nanayakkara, Three-dimensional-printable thermoactive helical interface with decentralized morphological stiffness control for continuum manipulators, IEEE Robot. Autom. Lett. 3 (3) (2018) 2283–2290.

[19] S. Wu, G.L. Baker, J. Yin, Y. Zhu, Fast thermal actuators for soft robotics, Soft Robot. 9 (6) (2022) 1031–1039.

[20] X. Huang, K. Kumar, M.K. Jawed, A. Mohammadi Nasab, Z. Ye, W. Shan, C. Majidi, Highly dynamic shape memory alloy actuator for fast moving soft robots, Adv. Mater. Technol. 4 (4) (2019) 1800540.

[21] M. Shahinpoor, Y. Bar-Cohen, J. Simpson, J. Smith, Ionic polymer-metal composites (IPMCs) as biomimetic sensors, actuators and artificial muscles-a review, Smart Mater. Struct. 7 (6) (1998) R15.

[22] Z. Jiang, P. Song, Strong and fast hydrogel actuators, Science 376 (6590) (2022) 245.

[23] L. Hines, K. Petersen, G.Z. Lum, M. Sitti, Soft actuators for small-scale robotics, Adv. Mater. 29 (13) (2017) 1603483.

[24] W. Hu, G.Z. Lum, M. Mastrangeli, M. Sitti, Small-scale soft-bodied robot with multimodal locomotion, Nature 554 (7690) (2018) 81–85.

[25] C. Hong, Z. Ren, C. Wang, M. Li, Y. Wu, D. Tang, W. Hu, M. Sitti, Magnetically actuated gearbox for the wireless control of millimeter-scale robots, Sci. Robot. 7 (69) (2022) eabo4401.

[26] T. Wang, H. Ugurlu, Y. Yan, M. Li, M. Li, A.-M. Wild, E. Yildiz, M. Schneider, D. Sheehan, W. Hu, et al., Adaptive wireless millirobotic locomotion into distal vasculature, Nat. Commun. 13 (1) (2022) 4465.

[27] F. Xia, H. Wang, Y. Jia, Rediscovering black phosphorus as an anisotropic layered material for optoelectronics and electronics, Nat. Commun. 5 (1) (2014) 4458.

[28] E. Acome, S.K. Mitchell, T. Morrissey, M. Emmett, C. Benjamin, M. King, M. Radakovitz, C. Keplinger, Hydraulically amplified self-healing electrostatic actuators with muscle-like performance, Science 359 (6371) (2018) 61–65.

[29] Z. Yoder, D. Macari, G. Kleinwaks, I. Schmidt, E. Acome, C. Keplinger, A soft, fast and versatile electrohydraulic gripper with capacitive object size detection, Adv. Funct. Mater. 33 (3) (2023) 2209080.

[30] T. Park, K. Kim, S.-R. Oh, Y. Cha, Electrohydraulic actuator for a soft gripper, Soft Robot. 7 (1) (2020) 68–75.

[31] E. Leroy, R. Hinchet, H. Shea, Multimode hydraulically amplified electrostatic actuators for wearable haptics, Adv. Mater. 32 (36) (2020) 2002564.

[32] A.K. Han, S. Ji, D. Wang, M.R. Cutkosky, Haptic surface display based on miniature dielectric fluid transducers, IEEE Robot. Autom. Lett. 5 (3) (2020) 4021–4027.

[33] N. Kellaris, P. Rothemund, Y. Zeng, S.K. Mitchell, G.M. Smith, K. Jayaram, C. Keplinger, Spider-inspired electrohydraulic actuators for fast, soft-actuated joints, Adv. Sci. 8 (14) (2021) 2100916.

[34] R. Chen, Z. Yuan, J. Guo, L. Bai, X. Zhu, F. Liu, H. Pu, L. Xin, Y. Peng, J. Luo, et al., Legless soft robots capable of rapid, continuous, and steered jumping, Nat. Commun. 12 (1) (2021) 7028.

[35] T. Wang, H.-J. Joo, S. Song, W. Hu, C. Keplinger, M. Sitti, A versatile jellyfish-like robotic platform for effective underwater propulsion and manipulation, Sci. Adv. 9 (15) (2023) eadg0292.

[36] B. Johnson, M. Naris, V. Sundaram, A. Volchko, K. Ly, S. Mitchell, E. Acome, N. Kellaris, C. Keplinger, N. Correll, et al., A multifunctional soft robotic shape display with high-speed actuation, sensing, and control, Nat. Commun. 14 (1) (2023) 4516.

[37] M. Taghavi, T. Helps, J. Rossiter, Electro-ribbon actuators and electro-origami robots, Sci. Robot. 3 (25) (2018) eaau9795.

[38] M.N. Zadeh, M. Garrad, C. Romero, A. Conn, F. Scarpa, J. Rossiter, Robo-Heart: a bi-directional zipping actuator, IEEE Robot. Autom. Lett. 7 (4) (2022) 10352–10358.

[39] W. Sun, Y. Xu, M. Taghavi, A flexi-limbed electroactive frame for gripping and locomotion: Structural optimization, Int. J. Mech. Sci. (2024) 109862.

[40] R.S. Diteesawat, T. Helps, M. Taghavi, J. Rossiter, Electro-pneumatic pumps for soft robotics, Sci. Robot. 6 (51) (2021) eabc3721.

[41] Q. He, S. Cai, Soft pumps for soft robots, Sci. Robot. 6 (51) (2021) eabg6640.

[42] X. Wang, Y. Wang, M. Zhu, X. Yue, 2-dimensional impact-damping electrostatic actuators with elastomer-enhanced auxetic structure, Nat. Commun. 15 (1) (2024) 7333.

[43] Y. Xu, E. Burdet, M. Taghavi, Electromechanical model for electro-ribbon actuators, Int. J. Mech. Sci. 275 (2024) 109340.

[44] B. Castro, R.S. Diteesawat, M. Taghavi, J. Rossiter, Modular simulation framework for electro-ribbon actuators, in: 2021 IEEE 4th International Conference on Soft Robotics, RoboSoft, IEEE, 2021, pp. 215–221.

[45] T. Helps, C. Romero, M. Taghavi, A.T. Conn, J. Rossiter, Liquid-amplified zipping actuators for micro-air vehicles with transmission-free flapping, Sci. Robot. 7 (63) (2022) eabi8189.

[46] J.H. Chong, C. Romero, M. Taghavi, J. Rossiter, Electro-ribbon muscles for biomimetic wing flapping, in: 2022 IEEE 5th International Conference on Soft Robotics, RoboSoft, IEEE, 2022, pp. 638–643.

[47] R. Legtenberg, J. Gilbert, S.D. Senturia, M. Elwenspoek, Electrostatic curved electrode actuators, J. Microelectromech. Syst. 6 (3) (1997) 257–265.

[48] B. Preetham, M.A. Lake, D.J. Hoelzle, A curved electrode electrostatic actuator designed for large displacement and force in an underwater environment, J. Micromech. Microeng. 27 (9) (2017) 095009.

[49] M. Hsu, et al., Deflection analysis of electrostatic micro-actuators using the differential quadrature method, J. Appl. Sci. Eng. 9 (2) (2006) 97–106.

[50] A.K. Chinthakindi, D. Bhusari, B.P. Dusch, J. Musolf, B.A. Willemsen, E. Prophet, M. Roberson, P.A. Kohl, Electrostatic actuators with intrinsic stress gradient: I. Materials and structures, J. Electrochem. Soc. 149 (8) (2002) H139.

[51] J.H. Kuang, C.J. Chen, The nonlinear electrostatic behavior for shaped electrode actuators, Int. J. Mech. Sci. 47 (8) (2005) 1172–1190.

[52] S.P. Burugupally, D. Hoelzle, Experimental investigation of curved electrode actuator dynamics in viscous dielectric media, Appl. Phys. Lett. 113 (7) (2018).

[53] S.P. Burugupally, Mechanics of a curved electrode actuator operating in viscous dielectric media: Simulation and experiment, J. Micro-Bio Robot. 15 (1) (2019) 43–51.

[54] M. Elwenspoek, L. Smith, B. Hok, Active joints for microrobot limbs, J. Micromech. Microeng. 2 (3) (1992) 221.

[55] N. Lange, F. Wippermann, E. Beckert, R. Eberhardt, A. Tünnermann, Polymer-based pull-in free electrostatic microactuators fabricated on wafer-level, J. Microelectromech. Syst. 24 (4) (2014) 949–957.

[56] M.A. Rosa, D. De Bruyker, A.R. Völkel, E. Peeters, J. Dunec, A novel external electrode configuration for the electrostatic actuation of MEMS based devices, J. Micromech. Microeng. 14 (4) (2004) 446.

[57] R. Coelho, Physics of Dielectrics for the Engineer, Vol. 1, Elsevier, 2012.

[58] V.I. Gibalov, G.J. Pietsch, The development of dielectric barrier discharges in gas gaps and on surfaces, J. Phys. D: Appl. Phys. 33 (20) (2000) 2618.

[59] B.M. Goldberg, I. Shkurenkov, I.V. Adamovich, W.R. Lempert, Electric field in an AC dielectric barrier discharge overlapped with a nanosecond pulse discharge, Plasma Sources Sci. Technol. 25 (4) (2016) 045008.

[60] C. Guo, F. Tang, J. Chen, X. Wang, S. Zhang, X. Zhang, Development of dielectric-barrier-discharge ionization, Anal. Bioanal. Chem. 407 (2015) 2345–2364.

[61] X. Xu, Dielectric barrier discharge-properties and applications, Thin Solid Films 390 (1–2) (2001) 237–242.

[62] B. Eliasson, W. Egli, U. Kogelschatz, Modelling of dielectric barrier discharge chemistry, Pure Appl. Chem. 66 (6) (1994) 1275–1286.

[63] T.C. Corke, C.L. Enloe, S.P. Wilkinson, Dielectric barrier discharge plasma actuators for flow control, Annu. Rev. Fluid Mech. 42 (1) (2010) 505–529.

[64] W.S. Kang, J.M. Park, Y. Kim, S.H. Hong, Numerical study on influences of barrier arrangements on dielectric barrier discharge characteristics, IEEE Trans. Plasma Sci. 31 (4) (2003) 504–510.

[65] J.H. Choi, I. Han, H.K. Baik, M.H. Lee, D.-W. Han, J.-C. Park, I.-S. Lee, K.M. Song, Y.S. Lim, Analysis of sterilization effect by pulsed dielectric barrier discharge, J. Electrost. 64 (1) (2006) 17–22.

[66] B. Jayaraman, W. Shyy, Modeling of dielectric barrier discharge-induced fluid dynamics and heat transfer, Prog. Aerosp. Sci. 44 (3) (2008) 139–191.

[67] N.D. Wilde, H. Xu, N. Gomez Vega, S.R. Barrett, A model of surface dielectric barrier discharge power, Appl. Phys. Lett. 118 (15) (2021).

[68] U. Kogelschatz, Dielectric-barrier discharges: their history, discharge physics, and industrial applications, Plasma Chem. Plasma Process. 23 (1) (2003) 1–46.

[69] J. Shang, Electromagnetic field of dielectric barrier discharge, in: 36th AIAA Plasmadynamics and Lasers Conference, 2005, p. 5182.

[70] A.H. Nayfeh, Linear and Nonlinear Structural Mechanics, John Wiley & Sons, 2008.

[71] P.G. Gennes, F. Brochard Wyart, D. Quéré, et al., Capillarity and Wetting Phenomena: Drops, Bubbles, Pearls, Waves, Springer, 2004.

[72] C. Mastrangelo, C. Hsu, Mechanical stability and adhesion of microstructures under capillary forces. II. Experiments, J. Microelectromech. Syst. 2 (1) (1993) 44–55.

[73] J. Liu, X. Feng, Capillary adhesion of microbeams: Finite deformation analysis, Chin. Phys. Lett. 24 (8) (2007) 2349–2352.

[74] J. Liu, X. Feng, R. Xia, H. Zhao, Hierarchical capillary adhesion of microcantilevers or hairs, J. Phys. D: Appl. Phys. 40 (18) (2007) 5564.

[75] L. Stollenwerk, J. Laven, H.-G. Purwins, Spatially resolved surface-charge measurement in a planar dielectric-barrier discharge system, Phys. Rev. Lett. 98 (25) (2007) 255001.

[76] O.D. Jefimenko, Correct use of Maxwell stress equations for electric and magnetic fields, Am. J. Phys. 51 (11) (1983) 988–996.